Available online at www.sciencedirect.com
ScienceDirect
Trans. Nonferrous Met. Soc. China 34(2024) 2828−2848
Transactions of Nonferrous Metals Society of China
www.tnmsc.cn

Micro-galvanic corrosion behaviour of Mg−(7,9)Al−1Fe−*x*Nd alloys

Kai-xuan FENG[1], Tao LAI[1], Yang CHEN[1], Zheng YIN[1],
Zhi-qin WU[1], Hong YAN[1], Hong-gun SONG[1], Chao LUO[1,2], Zhi HU[1]

1. School of Advanced Manufacturing, Nanchang University, Nanchang 330031, China;
2. Institute for Advanced Study, Nanchang University, Nanchang 330031, China

Received 14 February 2023; accepted 3 July 2023

Abstract: The localized micro-galvanic corrosion process and the kinetic information of Mg−(7,9)Al−1Fe−*x*Nd alloys were investigated by in situ observation under electrochemical control and in situ atomic force microscopy (AFM) in an electrolyte environment. The results revealed that the formation of the Nd-rich phase in alloys resulted in a decrease in the Volta potential difference from ~400 mV ($AlFe_3$/*α*-Mg) to ~220 mV (Nd-rich/*α*-Mg), reducing the corrosion products around the cathodic phase and corrosion current density of the microscale area. The addition of Nd significantly improved the corrosion resistance, mainly due to the suppression of the micro-galvanic corrosion between the second phases and substrate. Finally, the corrosion mechanism of Mg−(7,9)Al−1Fe−*x*Nd alloys was discussed based on in situ observations and electrochemical results.

Key words: magnesium alloy; scanning Kelvin probe force microscope; micro-galvanic corrosion; in situ observation; atomic force microscopy

1 Introduction

Magnesium (Mg) alloys are widely used in automotive, electronics, aviation, and restorative materials because they have a high specific strength, recyclability, electromagnetic shielding ability, and good bio-compatibility [1−5]. However, Mg alloys have poor corrosion resistance in chloride environments, significantly limiting their application range [6−9]. The main corrosion forms of Mg alloys are micro-galvanic corrosion, contact corrosion, pitting corrosion, filamentous corrosion and stress corrosion cracking in industry, such as marine atmospheric environments, acid, alkali, and salt solutions [10−14]. Galvanic corrosion is the most common and harmful form [15−17]. Therefore, it is critical to accurately characterize micro-galvanic corrosion behaviour in an electrolyte environment, which will help develop new corrosion-resistant Mg alloys.

In situ observation of corrosion was extremely important for revealing the mechanism of micro-galvanic corrosion. Many in situ monitoring techniques have been applied to investigating the corrosion behaviour of Mg alloys in an electrolyte environment [18−23]. In situ atomic force microscopy (AFM) was utilized to study the localized corrosion behaviour between the intermetallic phases and *α*-Mg matrix in flowing Hanks' solution [18]. The high spatial resolution of AFM accurately characterized and measured the corrosion morphology, which helped reveal the corrosion mechanism of Mg alloys at the microscale [8,15]. Considering the long scanning interval of the microprobe technique, it was highly necessary to study the corrosion process in combination with other more intuitive in situ

Corresponding author: Zhi HU, Tel: +86-791-83969633, E-mail: huzhi@ncu.edu.cn
DOI: 10.1016/S1003-6326(24)66579-9

observation techniques. In recent years, some in situ optical coupled with electrochemical techniques have successfully recorded the corrosion process and electrochemical kinetics of Mg alloys and other metals [24−27]. For example, laser scanning confocal microscopy (LSCM) coupled with an electrochemical technique revealed the pitting behaviour and corrosion kinetics information of duplex stainless steels in a LiBr solution [24]. LSCM enables in situ imaging of the corrosion process and provides essential insights during the initial corrosion stages in an electrolyte environment because of its high resolution. SHAO et al [27] used an in situ optical microscope (OM) to record the filiform corrosion process of AZ91D alloys and the corresponding potential−time curve in NaCl solutions during microscale polarization. The results indicated that the morphology of filiform corrosion was related to the microstructure, and corrosion extended along the α+β structure under galvanostatic polarization conditions. These in situ optical analyses combined with electrochemical techniques have directly and continuously revealed the electrochemical corrosion process, visualizing and quantifying the corrosion behaviour at the microscale. In addition to the above mentioned in situ corrosion monitoring methods, other in situ approaches, such as scanning vibrating electrode technique (SVET) and scanning ion-selective electrode technique (SIET), quasi-in situ scanning electron microscopy (SEM), and quasi-in situ transmission electron microscopy (TEM), have also been frequently utilized to investigate the corrosion behaviour of Mg alloys [20,28,29].

In our previous work [30], in situ AFM and quasi-in situ SEM results of Mg−9Al−1Fe−(Gd) alloys were presented, mainly focusing on the effect of nanoscale intermetallic phases on the corrosion process of Mg alloys in NaCl solution. The alloying of Fe and Gd amplified the micro-galvanic coupling effect, which helped investigate the corrosion mechanism of Mg−Al alloys [31−35]. According to in situ observation results, adding Gd weakened the micro-galvanic corrosion and suppressed the cathodic effect of the Fe-rich phase. Meanwhile, corrosion product deposition and cracking behaviour were discussed based on the in situ observation results. Although detailed insights into the micro-galvanic corrosion behaviour and the evolution of corrosion morphology of Mg alloys have been discussed, the real-time corrosion propagation behaviour and kinetics have not fully been understood yet. Inspired by this, this study adopted a similar alloy design method to further study the corrosion mechanism of Mg−Al alloys in a corrosive solution. Presently, the micro-galvanic corrosion behaviour and kinetics of Mg−(7,9)Al−1Fe−xNd (x=0, 0.4, 0.8, and 1.2 wt.%) alloys were investigated under electrochemical control in NaCl solution via in situ electrochemical OM technique. Besides, in situ AFM study was conducted to monitor the corrosion morphology of the nanoscale cathodic phase. The scanning Kelvin probe force microscope (SKPFM) and LSCM were combined to reveal the mechanism of micro-galvanic corrosion of the Mg−(7,9)Al−1Fe−xNd (x=0.4, 0.8, and 1.2 wt.%) alloy in NaCl solution.

2 Experimental

2.1 Materials and preparation precedure

Pure Mg (99.9 wt.%), pure Nd (99.9 wt.%) and Al−10wt.%Fe alloys were melted at 750 °C under the pure argon atmosphere. All raw materials were melted and held for 30 min to induce homogenization. The Mg−7Al−1Fe−xNd (x=0, 0.4, 0.8, and 1.2 wt.%) and Mg−9Al−1Fe−1Nd alloys were cast under gravity using a permanent mould with a diameter of 20 mm and cooled down naturally. The compositions of the tested alloys (Table 1) were obtained using inductively coupled plasma atomic emission spectrometry (ICP-AES; OPTIMA 5300DV).

Table 1 Compositions of Mg−7Al−1Fe−xNd (x=0, 0.4, 0.8, and 1.2 wt.%) and Mg−9Al−1Fe−1Nd alloys (wt.%)

Alloy	Al	Fe	Nd	Mn	Cu	Ni	Mg
Mg−7Al−1Fe	7.12	1.05	0	0.08	<0.001	<0.001	Bal.
Mg−7Al−1Fe−0.4Nd	6.87	0.95	0.41	0.12	<0.001	<0.001	Bal.
Mg−7Al−1Fe−0.8Nd	6.95	1.03	0.78	0.10	<0.001	<0.001	Bal.
Mg−7Al−1Fe−1.2Nd	7.04	0.98	1.22	0.13	<0.001	<0.001	Bal.
Mg−9Al−1Fe−1Nd	8.95	1.04	0.98	0.11	<0.001	<0.001	Bal.

2.2 Sample characterization

The microstructures of the tested alloys were observed by SEM (Quanta 200FEG) and TEM (Talos F200X). The samples were mechanically polished and etched with a 4 vol.% nitric acid solution for the observation of metallographic morphology. A precision ion polishing system (PIPS) was used to prepare the TEM samples until perforation.

The Volta potentials and morphologies of the tested alloys were characterized using a scanning Kelvin probe force microscope (SKPFM, Dimension ICON) in a tapping mode. The tapping mode eliminated most of the lateral forces, and the probability of sample surface damage was significantly reduced. The surface morphology and Volta potential maps were obtained under the dual-channel scanning mode. The topography was recorded using the tapping mode in the first scan, and the Volta potential was recorded at a probe-to-sample distance of 100 nm. All experiments were performed in a vibration isolation chamber at 25 °C with an approximate relative humidity of 40%.

2.3 Microscale potentiodynamic polarization and in situ observation

Figure 1 shows the in situ optical microscope (OM) equipment schematic under electrochemical control. An inverted optical microscope and an electrochemical workstation were subtly combined. The container for the in situ electrochemical OM experiment was 3D-printed with a thickness of 500 μm, and a thinner cover glass (170 μm) was used for the bottom observation area. This inverted, extremely thin in situ device facilitated microscale observations and protected the optical microscope lens. Subsequently, the container was connected to a potentiostat equipped with a three-electrode system consisting of a sample as the working electrode (~1 mm^2), a saturated calomel electrode as the reference electrode, and a platinum wire as the auxiliary electrode. The working electrode region exposed to the electrolyte was about 1000 μm × 1000 μm. Except for the electrode area, the remaining sample area was covered with epoxy resin and polyimide tape. All specimens were immersed in a 0.01 mol/L NaCl solution for 10 min at an open circuit potential (OCP). The initial potential was −0.2 V (vs OCP) with a scanning rate of 2 mV/s.

In situ AFM experiments were conducted using atomic force microscopy (AFM, Agilent 5500), similar to the device designed by SHEN et al [30]. The sample was immersed in a circulating electrolyte that was exposed to air. After immersion in the electrolyte circulation system, AFM was used to record the initial morphology

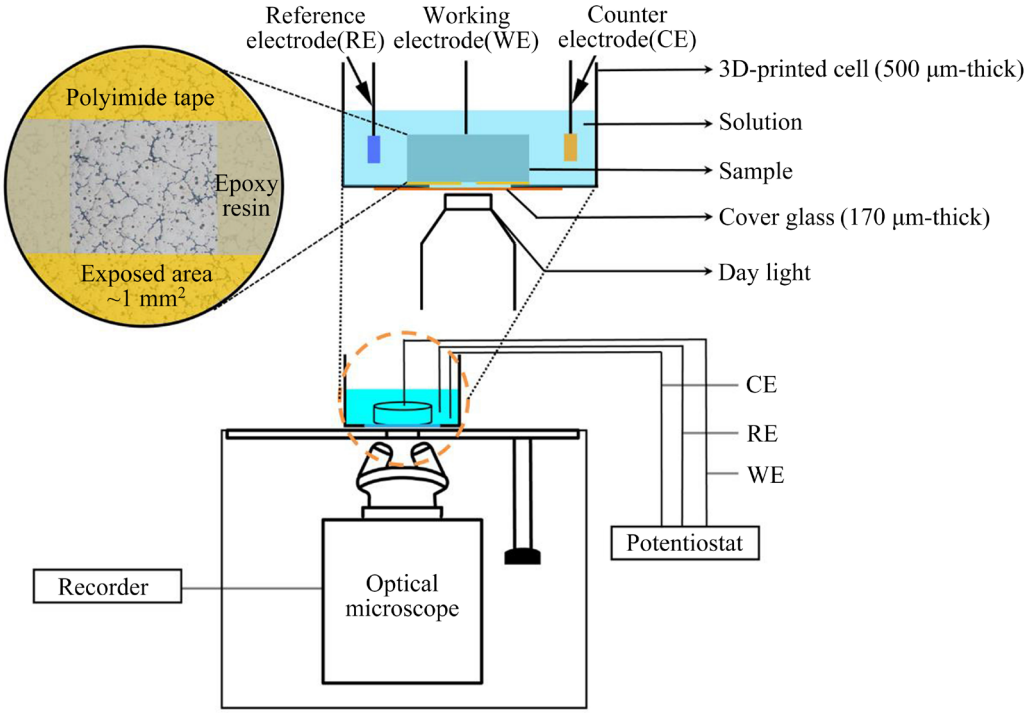

Fig. 1 In situ OM experimental setup under electrochemical control

map. A topographic map at the same position was re-recorded after immersion for 30 min. In situ LSCM and OM tests were performed with a laser scanning confocal microscope (Zeiss 710) and an optical microscope (Nikon MA200), respectively. In situ OM monitoring was conducted in 0.6 mol/L NaCl solution, and a succession of pictures were recorded. Moreover, a position mark was carefully made on the surface of the samples during in situ OM experiments so that the observed areas could be accurately relocated to track and monitor. The initial and final surface morphologies at the same position were recorded using SEM.

2.4 Electrochemical tests

The electrochemical measurements were conducted on a Princeton P4000 electrochemistry workstation that was connected to a three-electrode electrolytic cell. Before the polarization and EIS measurements, an OCP was detected in 0.6 mol/L NaCl solution for 10 min to ensure a steady test environment. The three-electrode system was consistent with that of the in situ electrochemical test. The polarization curve was measured at a scanning rate of 1 mV/s in the range from −250 to 250 mV (vs OCP). The EIS frequency ranged from 10^5 to 10^{-1} Hz, and the perturbation amplitude was 5 mV (vs OCP). Versa Studio and ZView softwares were used to analyze the polarization curves and EIS data.

2.5 Immersion tests

Hydrogen evolution and mass loss tests were conducted in 0.6 mol/L NaCl solution. The released hydrogen gas was continuously collected using an inverted funnel and burette, and five parallel samples were collected to obtain reliable data. As the Fe-containing alloys exhibited a fast corrosion rate, it was difficult for the burette to collect so much gas. Hence, different immersion time was set (24 h for the Mg−7Al−1Fe−*x*Nd alloys (*x*=0.4, 0.8, and 1.2 wt.%) and 10 h for Mg−7Al−1Fe alloy). After immersion in chromate solution (200 g/L CrO_3 + 10 g/L $AgNO_3$) for 10 min to remove the surface corrosion products and to dry in the air, the mass loss results were determined and corrected using the evaluated results. The corrosion rates of the hydrogen evolution (P_H, mm/a) and mass loss (P_W, mm/a) were calculated as follows [36]:

$$P_H = 2.279\frac{H_i - H_f}{At} \quad (1)$$

$$P_W = 2.10\frac{m_i - m_f}{At} \quad (2)$$

where H_i (mL) and H_f (mL) are the initial and final numerical values of the burette, respectively; m_i (mg) and m_f (mg) are the initial and final masses, respectively; A (cm^2) is the surface area; t (d) is the immersion time.

The chemical states of the alloying elements in the corrosion products were analyzed using X-ray photoelectron spectroscopy (XPS) with monochromatic Al K_α radiation (1486.6 eV). The C 1s peak (284.8 eV) was used to standardize the binding energy. The Avantage software was used to fit the XPS results.

3 Results

3.1 Microstructure

Figure 2 shows the surface morphology and corresponding EDS mappings of the Mg−7Al−1Fe−*x*Nd alloys (*x*=0, 0.4, 0.8, and 1.2 wt.%) and Mg−9Al−1Fe−1Nd alloy. As shown in Figs. 2(a) and (b), the Mg−7Al−1Fe alloy was composed of *α*-Mg matrix, *β*-$Mg_{17}Al_{12}$ phase, and Al−Fe intermetallic particles. It can be seen from elemental distribution maps shown in Fig. 2(c) that the silver-white particle (Fig. 2(b)) was mainly enriched in Al and Fe elements, indicating that the white granular phase included the Al−Fe intermetallic compound. The microstructures of the Mg−(7,9)Al−1Fe alloy with different Nd contents are shown in Figs. 2(d−o). It can be seen that some white particles appeared (Figs. 2(d−f)), and the number of these particles gradually increased with increasing Nd content (Figs. 2(g−n)). According to the corresponding EDS mapping results (Figs. 2(f, i, l, o)), the white phase in the alloys was enriched in Al and Nd, and most Fe was distributed uniformly. Therefore, the white phase was preliminarily identified as the Nd-rich phase. With the addition of Nd, excessive Al was consumed, leading to a decrease in the Al element forming *β*-$Mg_{17}Al_{12}$, and the morphology of the *β*-$Mg_{17}Al_{12}$ phase became fine and dispersed, as shown in Figs. 2(d−o).

TEM analysis was performed to further determine the phase composition of the Mg−(7,9)Al−1Fe−(0.8Nd) alloys, as shown in Fig. 3. It

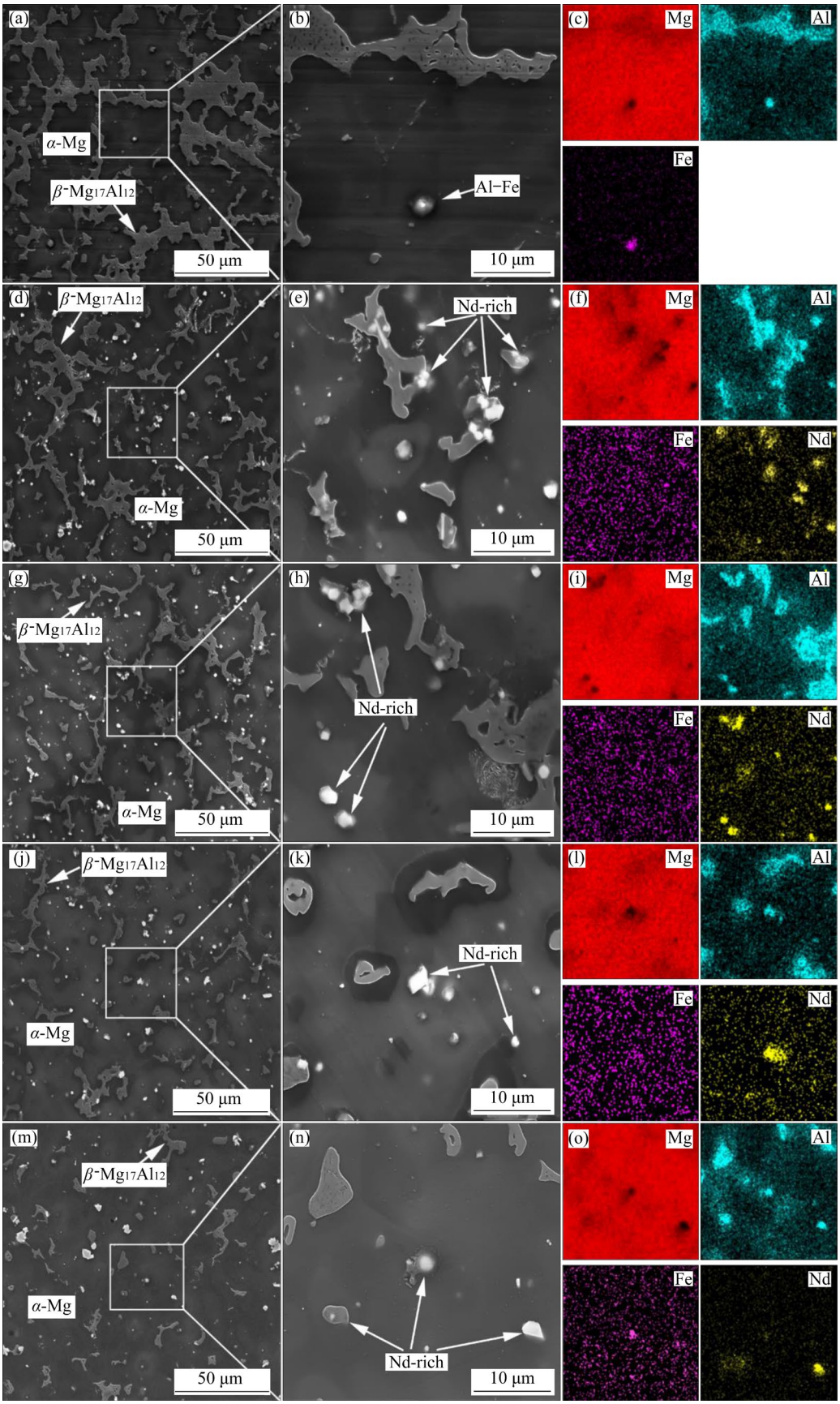

Fig. 2 SEM images (a, b, d, e, g, h, j, k, m, n) and corresponding EDS mappings (c, f, i, l, o) of tested alloys: (a−c) Mg−7Al−1Fe; (d−f) Mg−7Al−1Fe−0.4Nd; (g−i) Mg−7Al−1Fe−0.8Nd; (j−l) Mg−7Al−1Fe−1.2Nd; (m−o) Mg−9Al−1Fe−1Nd

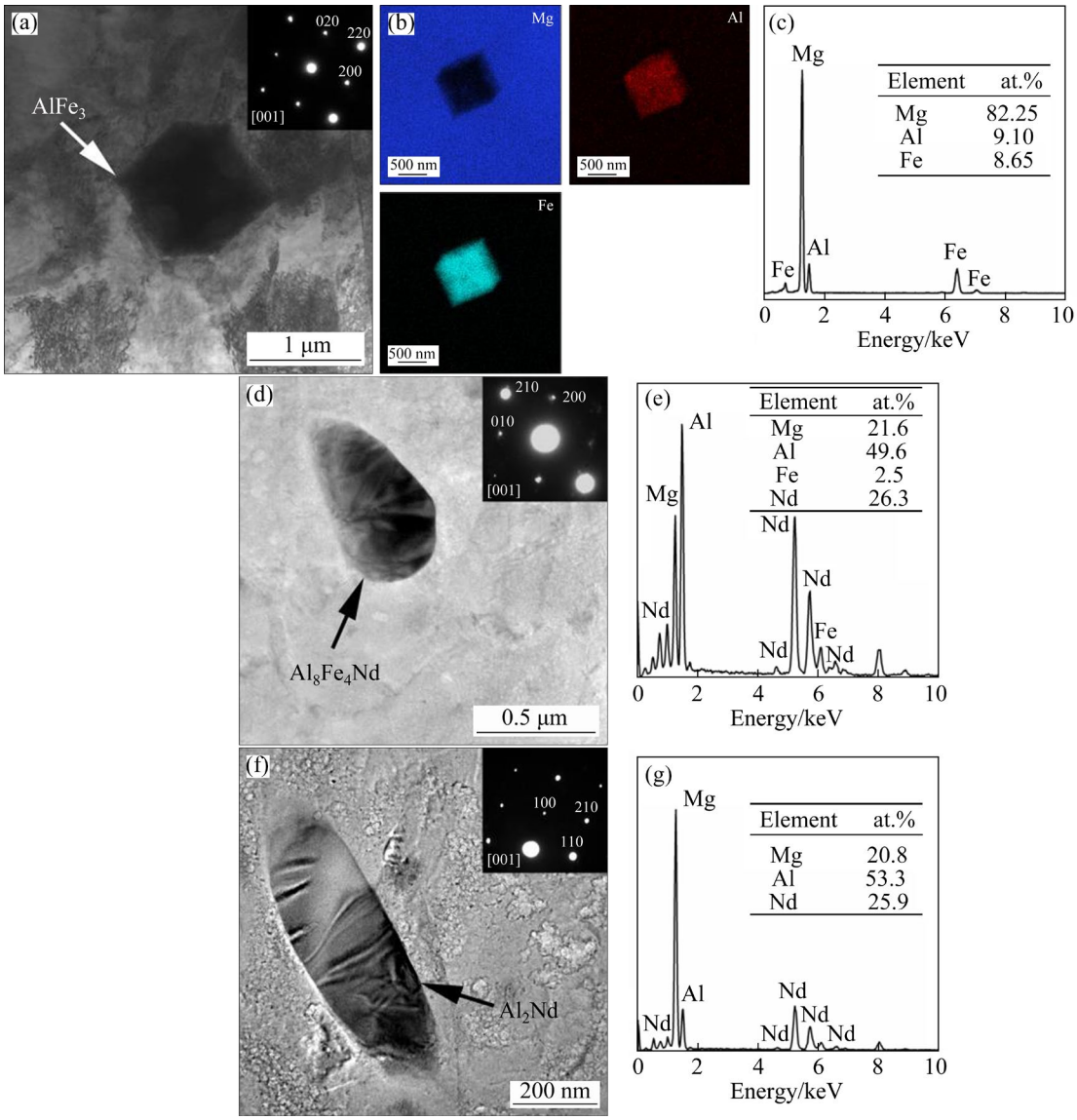

Fig. 3 TEM bright field images (a, d, f) and EDS results (b, c, e, g) of second phase particles in Mg−7Al−1Fe (a−c) and Mg−7Al−1Fe−0.8Nd (d−g) alloys: (a−c) $AlFe_3$; (d, e) Al_8Fe_4Nd; (f, g) Al_2Nd

can be seen that $AlFe_3$ phase (Fig. 3(a)) is detected in Mg−7Al−1Fe alloys (face-centred cubic structure, $a=b=c$=5.815 Å). Furthermore, the scanning energy spectrum and EDS results in Figs. 3(b) and (c) also confirmed the existence of the $AlFe_3$ phase. Figure 3(d) shows a TEM bright field image of the Al_8Fe_4Nd phase and SAED pattern. The diffraction patterns of this phase could be consistently indexed to Al_8Fe_4Nd ($a=b$=8.789 Å; c=5.054 Å). Figure 3(e) mainly consists of Mg, Al and Nb elements, with small amounts of Fe in the EDS results. In addition, a block-shaped particle with a size of 200 nm was detected, as shown in Fig. 3(f). According to the corresponding SAED pattern and EDS results (Fig. 3(g)), the block-shaped phase is Al_2Nd (face-centred cubic structure, $a=b=c$=8.000 Å). According to TEM results in Fig. 3, the Al−Fe phase and Al−(Fe)−Nd phases can be identified as $AlFe_3$, Al_8Fe_4Nd, and Al_2Nd phases, respectively.

3.2 In situ observation results

SKPFM and in situ LSCM results for the Mg−7Al−1Fe alloy are shown in Fig. 4. As shown in Figs. 4(a) and (b), the 2D and 3D topographies display white blocky $AlFe_3$ and continuous network of the β-$Mg_{17}Al_{12}$ phases. Figures 4(c) and (d) clearly show a significant Volta potential difference between the $AlFe_3$ and α-Mg phases (~400 mV), whereas the difference between the β-$Mg_{17}Al_{12}$ and α-Mg matrix is ~140 mV. This suggests that an

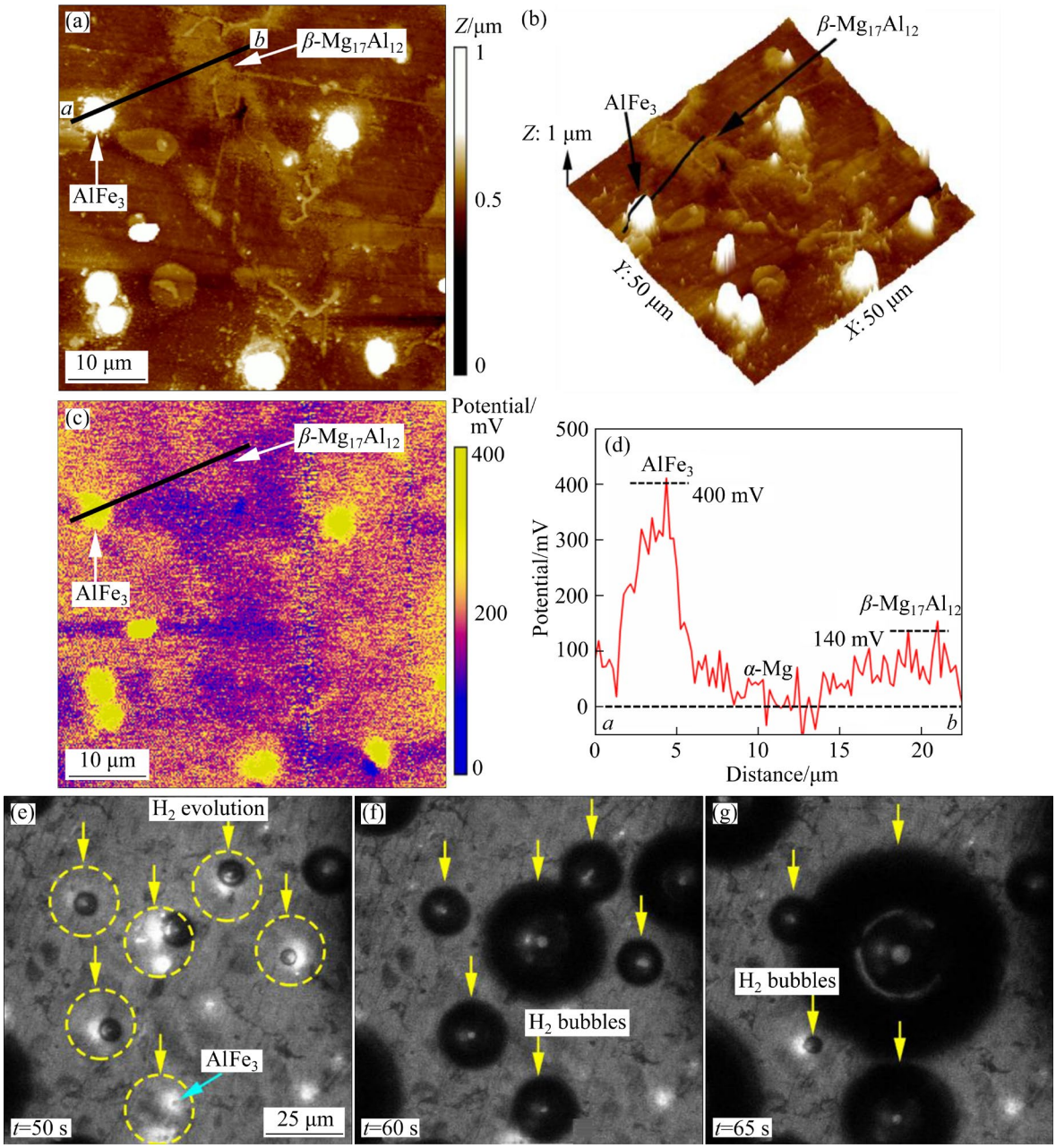

Fig. 4 SKPFM (a−d) and in situ LSCM (e−g) results of Mg−7Al−1Fe alloy: (a) 2D topography; (b) 3D topography; (c) Volta potential map; (d) Relative Volta potential profile; (e−g) Initial corrosion morphology changes of Mg−7Al−1Fe alloy with time in 0.6 mol/L NaCl solution, obtained by means of in situ LSCM

intense galvanic couple was formed between the $AlFe_3$ and α-Mg phases. Figures 4(e−g) show the initial corrosion behaviour of the Mg−7Al−1Fe alloy in 0.6 mol/L NaCl solution, obtained using in situ LSCM. It can be seen that some hydrogen bubbles were generated and expanded rapidly from the α-Mg matrix contiguous to the $AlFe_3$ phase with immersion time. The formation of hydrogen bubbles was associated with the cathode reactions ($2H_2O+2e=H_2\uparrow+2OH^-$), which reduced likelihood of acidic conditions, resulting in severe localized corrosion.

The topographic images and relative Volta potential linear profiles of the Mg−7Al−1Fe−0.8Nd alloys are shown in Fig. 5. The 2D and 3D topographies of the Mg−7Al−1Fe−0.8Nd alloy displayed a small dotted Nd-rich phase and β-$Mg_{17}Al_{12}$ phase, as depicted in Figs. 5(a) and (b). As shown in Figs. 5(c) and (d), the surface potential difference of the Nd-rich/α-Mg phase (~220 mV) was smaller than that of the $AlFe_3$/α-Mg phase (~400 mV) with the incorporation of Nd.

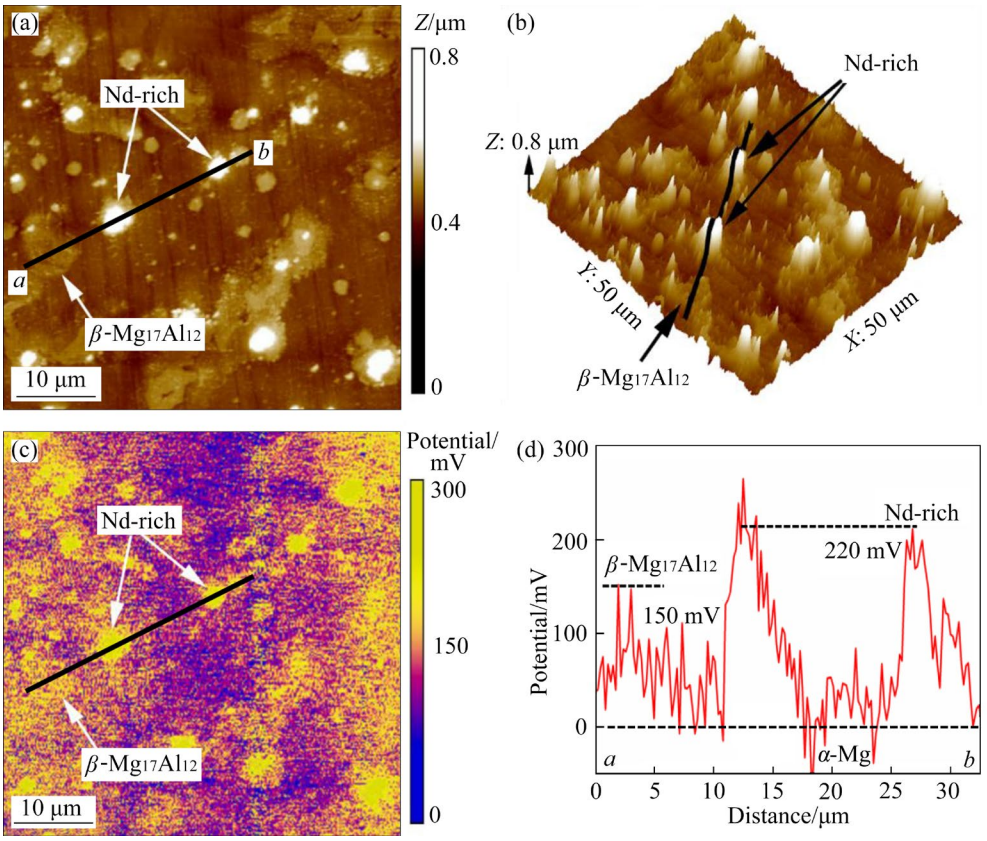

Fig. 5 SKPFM results of Mg−7Al−1Fe−0.8Nd alloy: (a) 2D topography; (b) 3D topography; (c) Volta potential map; (d) Relative Volta potential profile

Due to the excellent erosion resistance of the modified alloy, it was difficult to observe micro-galvanic corrosion using in situ LSCM. Therefore, the corrosion behaviour of the modified alloy was investigated using in situ AFM with a higher resolution. Figure 6 shows the morphology evolution of the Mg−9Al−1Fe−1Nd alloy in NaCl electrolyte with immersion time (0−30 min). Combined with the results of the microstructure and cross-section profile (Figs. 6(c−f)), the height of the β-$Mg_{17}Al_{12}$ and Nd-rich phases hardly changed after corrosion for 30 min. Notably, the cross-sectional profile between the β-$Mg_{17}Al_{12}$ and Nd-rich phases becomes higher, as shown in Fig. 6(f), indicating that a small amount of corrosion product is enriched in this position.

In order to facilitate in situ observations of the corrosion behaviour during the electrochemical polarization, in situ experiments under electrochemical control were performed in 0.01 mol/L NaCl. Figure 7 shows the microscale potentiodynamic polarization curves of the Mg−7Al−1Fe−(0.8Nd) alloys. Obviously, the corrosion potential (φ_{corr}) of the Mg−7Al−1Fe−0.8Nd alloy shifted positively, indicating that the corrosion driving force decreased. Moreover, the potentiodynamic polarization curve of Mg−7Al−1Fe−0.8Nd showed a wide passive region, in which the corrosion current density (J_{corr}) was much smaller than that of Mg−7Al−1Fe alloy. The J_{corr} in the passive region was approximately 10^{-5} A/cm^2, which depended on the transfer of ions by the oxide film. In the polarization curve of the Mg−7Al−1Fe alloy, the current density changed within an order of magnitude with the increase in potential in the region from Point 3 to Point 4, showing passivation characteristics. However, because of the high corrosion current density in this region (more than 6.6 mA/cm^2), it was not actual passivation but rather an area where uniform corrosion occurred rapidly. Current density fluctuation can be attributed to the formation and growth of metastable pits in the potentiodynamic polarization curves [21,37]. Pictures of the points where the current density fluctuated were further discussed, as shown in Fig. 8.

Figures 8(a−f) and (g−l) show the OM images of Mg−7Al−1Fe and Mg−7Al−1Fe−0.8Nd alloys

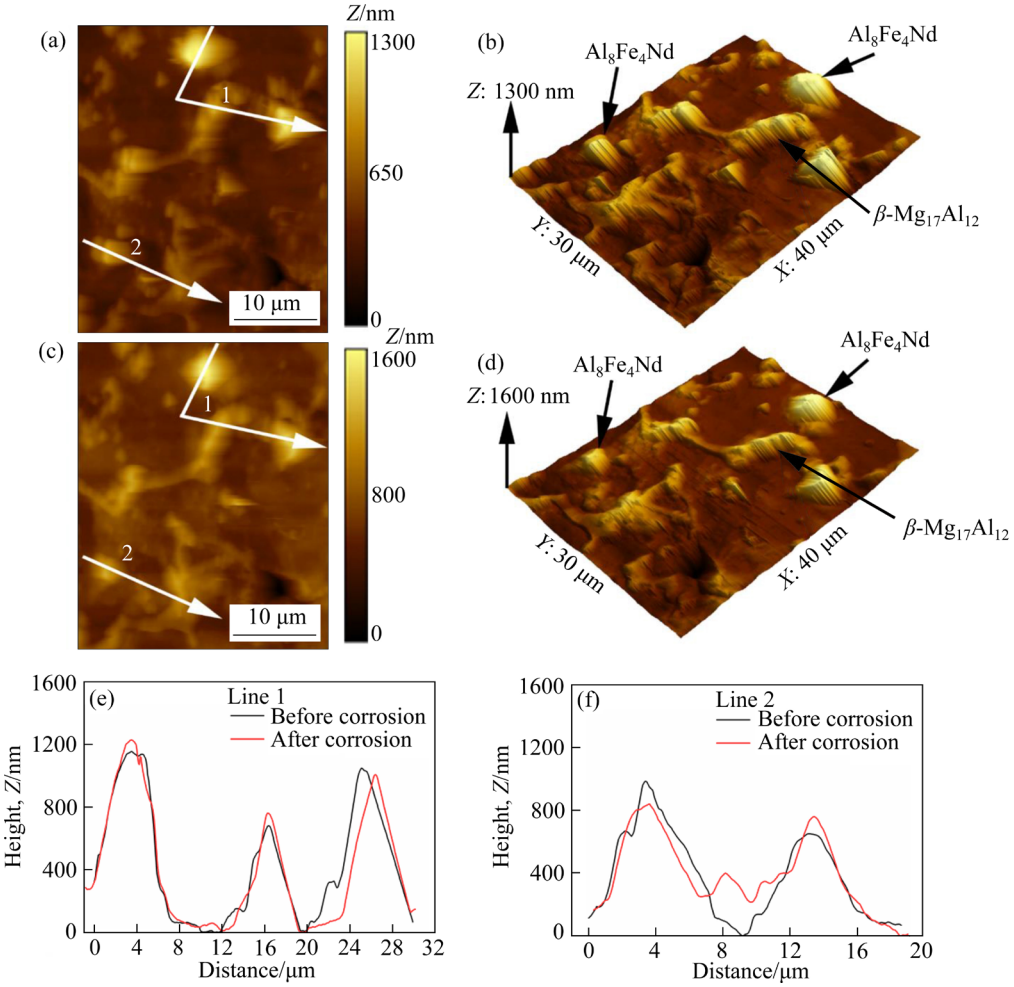

Fig. 6 In situ AFM corrosion morphology changes of Mg−9Al−1Fe−1Nd alloy with immersion time in 0.6 mol/L NaCl solution: (a, b) Before corrosion; (c, d) After 30 min of exposure to 0.6 mol/L NaCl solution; (e, f) Height profiles for Lines 1 and 2 in (a) and (c) showing topographical changes, respectively

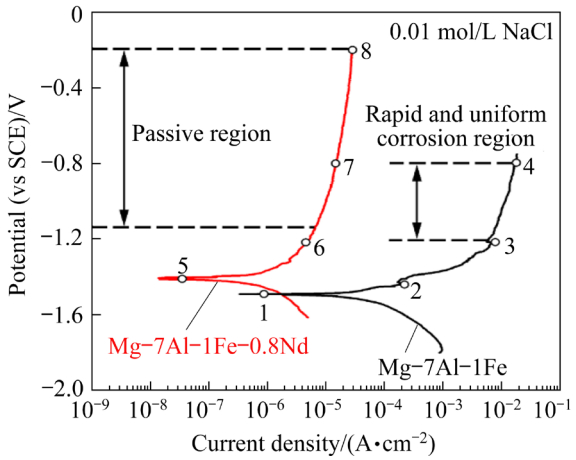

Fig. 7 Microscale potentiodynamic polarization curves of Mg−7Al−1Fe−(0.8Nd) alloys with scan rate of 2 mV/s in 0.01 mol/L NaCl solution (open to air)

during microscale potentiodynamic polarization in 0.01 mol/L NaCl at the points indicated in Fig. 7, respectively. Points 1−8 in Fig. 8 correspond to the white dot marks 1−8 in Fig. 7. In Fig. 8(a), the particles observed were the $AlFe_3$ phase in the Mg−7Al−1Fe alloy, indicated by the yellow arrows. Subsequently, some bubbles were generated from the α-Mg contiguous to the $AlFe_3$ phase in Fig. 8(b) (t=153 s), corresponding to the site marked by Point 1 in Fig. 7. Subsequently, these bubbles constantly expanded and merged with time from 153 to 292 s, as shown in Figs. 8(b−d). The corresponding corrosion current density J_{corr} increased from 3.2 to 6.6 mA/cm^2. Figure 8(e) corresponds to Point 4 in Fig. 7, where J_{corr} reached 17.1 mA/cm^2. Severe filiform corrosion occurred at 497 s, as shown in Fig. 8(e). After polarization, it can be observed from Fig. 8(f) that the filiform corrosion spread along the β-$Mg_{17}Al_{12}$ phase, and various corrosion pits formed near the $AlFe_3$ particles. Interestingly, the β-$Mg_{17}Al_{12}$ phase prevented the spread of filiform corrosion, which

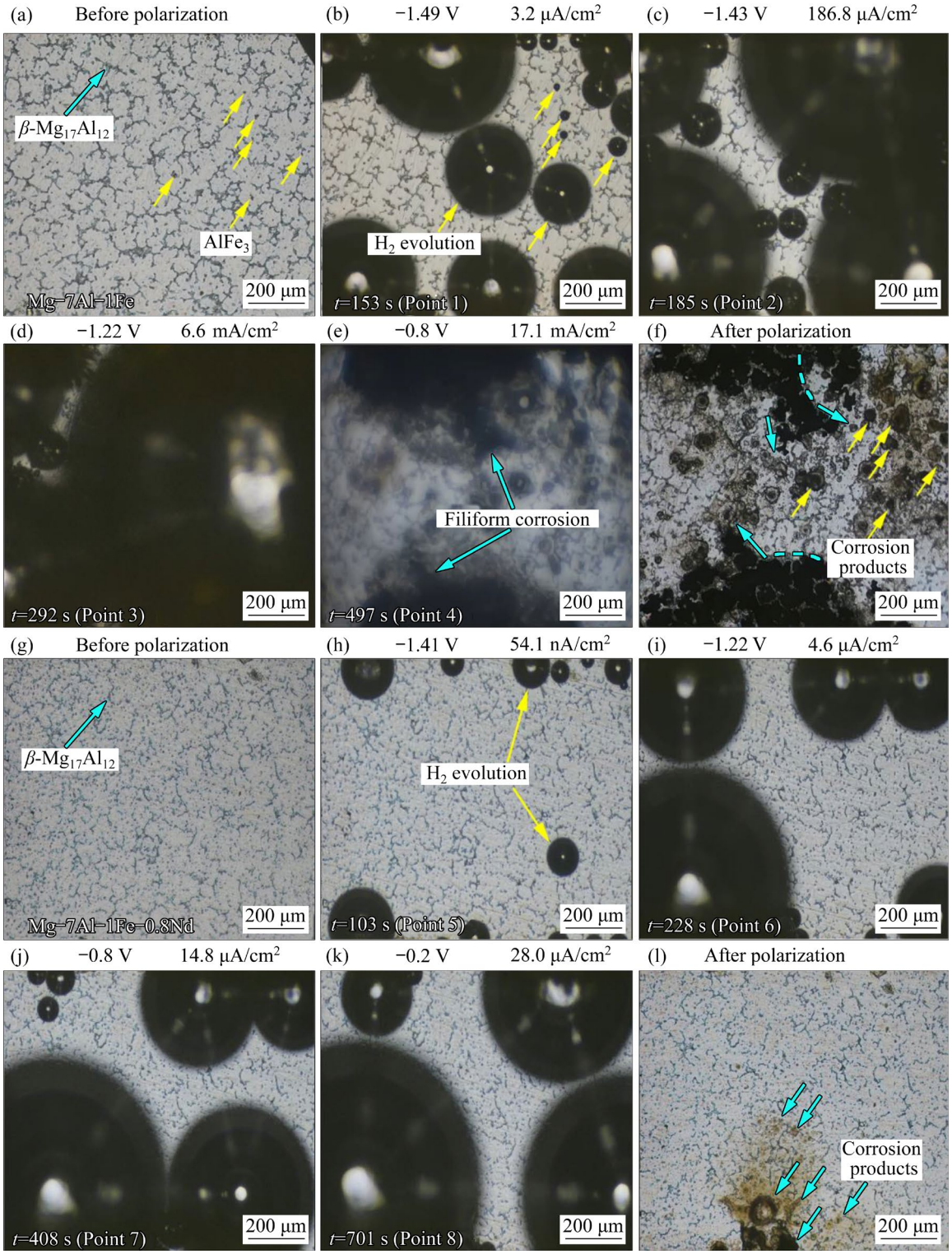

Fig. 8 OM images of Mg−7Al−1Fe−(0.8Nd) alloys during microscale potentiodynamic polarization in 0.01 mol/L NaCl at points indicated in Fig. 7: (a–f) Mg−7Al−1Fe alloy; (g–l) Mg−7Al−1Fe−0.8Nd alloy

can be attributed to the continuous network structure of the β-$Mg_{17}Al_{12}$ phase [27].

Figure 8(g) shows an OM image of Mg−7Al−1Fe−0.8Nd before polarization, and the fine Nd-rich phase was distributed between β-$Mg_{17}Al_{12}$ phases. As shown in Fig. 8(h), few H_2 bubbles were generated in the image, and J_{corr} was only 54.1 nA/cm^2. Consequently, the J_{corr} increased from 4.6 to 28.0 μA/cm^2 when the corrosion potential increased from −1.22 to −0.2 V (vs SCE)

in Figs. 8(i−k). During potentiodynamic polarization, there was no apparent corrosion attack with an increase in immersion time. According to the OM image after polarization (Fig. 8(l)), it was concluded that most areas of the alloy were not corroded, and only a small amount of corrosion products were formed locally. By comparing the current density at the same potential (−1.22 and −0.8 V) with similar time scales, the corrosion current density J_{corr} of the Mg−7Al−1Fe−0.8Nd alloy is three orders of magnitude smaller than that of Mg−7Al−1Fe alloy, as shown in Figs. 8(d, e) and Figs. 8(i, j). The corresponding in situ OM image during the potentiodynamic polarization experiment showed that the corrosion current density value reached 17.1 mA/cm^2 when the filiform corrosion extended along the β-$Mg_{17}Al_{12}$ phase with a large number of bubbles, as shown in Fig. 8(e). In contrast, in the Mg−7Al−1Fe−0.8Nd alloy, only a few areas of slight corrosion occurred on the surface, accompanied with a small number of H_2 bubbles. The potentiodynamic polarization curve of Mg−7Al−1Fe−0.8Nd also showed a wide passivation region during the in situ electrochemical test, and the current density was maintained in the range of 4.6−28.0 μA/cm^2, which was much lower than that of Mg−7Al−1Fe alloy.

In situ OM corrosion observation was performed to further investigate the localized microgalvanic behaviour and corrosion morphology changes at the same position of Mg−7Al−1Fe alloy in 0.6 mol/L NaCl solution, as shown in Figs. 9(a−f).

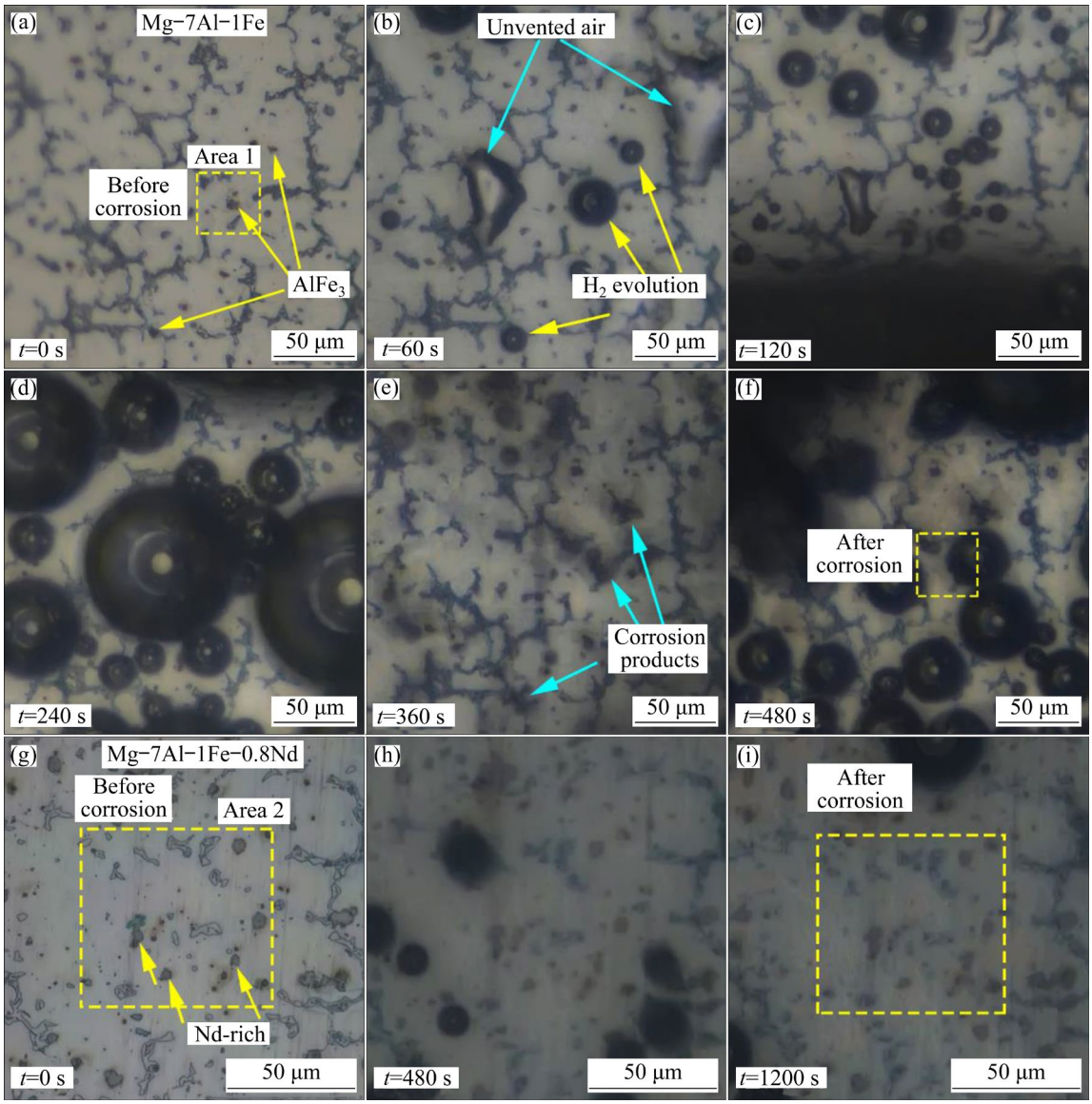

Fig. 9 OM images showing corrosion morphology changes of Mg−7Al−1Fe−(0.8Nd) alloys with immersion time in 0.6 mol/L NaCl solution: (a−f) Mg−7Al−1Fe alloy; (g−i) Mg−7Al−1Fe−0.8Nd alloy

In the OM image before corrosion (Fig. 9(a)), granular $AlFe_3$ particles are distributed in the continuous network of the β-$Mg_{17}Al_{12}$ phase. As shown in Fig. 9(b), several H2 bubbles emerged around the $AlFe_3$ phases during the initial stage of corrosion (t=60 s). Subsequently, an abundance of H_2 bubbles were generated, and the size of the bubbles increased with the increase time, eventually converging into large H_2 bubbles on the surface of the sample, as shown in Figs. 9(c) and (d). The entire process can be summarised as follows: H_2 bubbles form, grow, burst, and reproduce. Figure 9(e) shows severe corrosion around the $AlFe_3$ phases, whereas the β-$Mg_{17}Al_{12}$ phase did not change significantly. The experiment was terminated at 480 s (Fig. 9(f)) because the corrosion was too severe to continue the observation. Figures 9(g−i) show the corrosion process of the Mg−7Al−1Fe−0.8Nd alloy. In Fig. 9(g), the dark grey particles indicated by yellow arrows represent the Nd-rich phase. The β-$Mg_{17}Al_{12}$ phase became fine and dispersed because of the consumption of Al by the Nd-rich phase. As seen in Fig. 9(h) (t=480 s), there was almost no change of the Mg−7Al−1Fe−0.8Nd alloy, except for a few H_2 bubbles emerging from the Nd-rich phase. Notably, there was no apparent corrosion attack on the sample appearance with increasing immersion time, as shown in Fig. 9(i).

Figures 10(a−c) and (d−f) show the OM and SEM images of the Mg−7Al−1Fe alloy before and after corrosion, corresponding to the rectangular areas in Figs. 9(a) and (f), respectively. A comparison of the SEM images (Figs. 10(b) and (e)) shows that severe corrosion occurred at the $AlFe_3$/α-Mg interface. A lot of white corrosion products were formed near the $AlFe_3$ phase and a few around the β-$Mg_{17}Al_{12}$ phase (Fig. 10(e)). It can be observed that O was mainly enriched around the $AlFe_3$ phase, whereas Al hardly changed (Figs. 10(c) and (f)). Figures 10(g−i) and (j−m) show the OM and SEM images of the Mg−7Al−1Fe−0.8Nd alloy before and after corrosion, corresponding to the rectangular areas in Figs. 9(g) and (i), respectively. The Nd-rich phase in Fig. 10(h) did not exhibit slight corrosion until 1200 s (Fig. 10(k)). The corresponding EDS results (Figs. 10(l) and (m)) show that O was mainly enriched around the Nd-rich phase, indicating that some oxides were generated, whereas there was no significant change near the β-$Mg_{17}Al_{12}$ phase. Figures 10(n) and (o) show high-magnification corrosion film images of Mg−7Al−1Fe−(0.8Nd) alloys, corresponding to the rectangular areas in Figs. 10(e) and (k), respectively. The corrosion film of Mg−7Al−1Fe (Fig. 10(n)) was loose and porous, and some cracks existed in the corrosion film. In contrast, the corrosion film of Mg−7Al−1Fe−0.8Nd film (Fig. 10(o)) exhibited a dense staggered structure.

The surface corrosion product components of the Mg−7Al−1Fe−(0.8Nd) alloys after immersion in 0.6 mol/L NaCl solution were investigated using XPS, as shown in Fig. 11. The Mg 1s spectra (Figs. 11(a) and (b)) are divided into two peaks corresponding to Mg^{2+} and Mg, respectively. CO_3^{2-} was detected in Figs. 11(c−f), which might be attributed to the dissolved CO_2 in water. It was inferred that $Mg(OH)_2$ and $MgCO_3$ are in the corrosion products. The peak at 284.8 eV was consistent with C—C/C—H groups related to the adventitious hydrocarbons in the electrolyte [38]. The Nd 3d region (Fig. 11(g)) displayed the typical characteristics of Nd_2O_3 [39], and an energy loss peak was observed at 970 eV. Generally, the protective ability of an oxide film can be determined by the Pilling–Bedworth ratio (PBR), which is calculated as follows:

$$\mathrm{PBR}=\frac{V_{\mathrm{comp}}}{V_{\mathrm{M}}}=\frac{M_{\mathrm{comp}}\rho_{\mathrm{M}}}{nM\rho_{\mathrm{comp}}} \tag{3}$$

where V_{comp} and V_{M} represent the oxide volume and the metal volume consumed, respectively; ρ_{comp} and ρ_{M} are the corresponding densities; M_{comp} and n are the relative molecular mass of the oxide and number of metal atoms in the oxide, respectively, and M is the relative atomic mass of the metal. When the PBR value is between 1 and 2, the film is relatively dense and exhibits good protection. The film breaks easily because of the tensile or compressive stress when the PBR value is less than 1 or more than 2 [40]. The PBR of $Mg(OH)_2$, $MgCO_3$ and Nd_2O_3 are 1.8, 2.04, and 1.13, respectively. Because the PBR of $MgCO_3$ is greater than 2, it does not play a protective role. Though the PBR of $Mg(OH)_2$ is between 1 and 2, the porous structure of $Mg(OH)_2$ cannot act as a protective film. The PBR value of Nd_2O_3 (1.13) suggests that it can act as a stable and dense protective film. The corrosion film containing Nd_2O_3 in the Mg−7Al−1Fe−0.8Nd alloy can effectively isolate

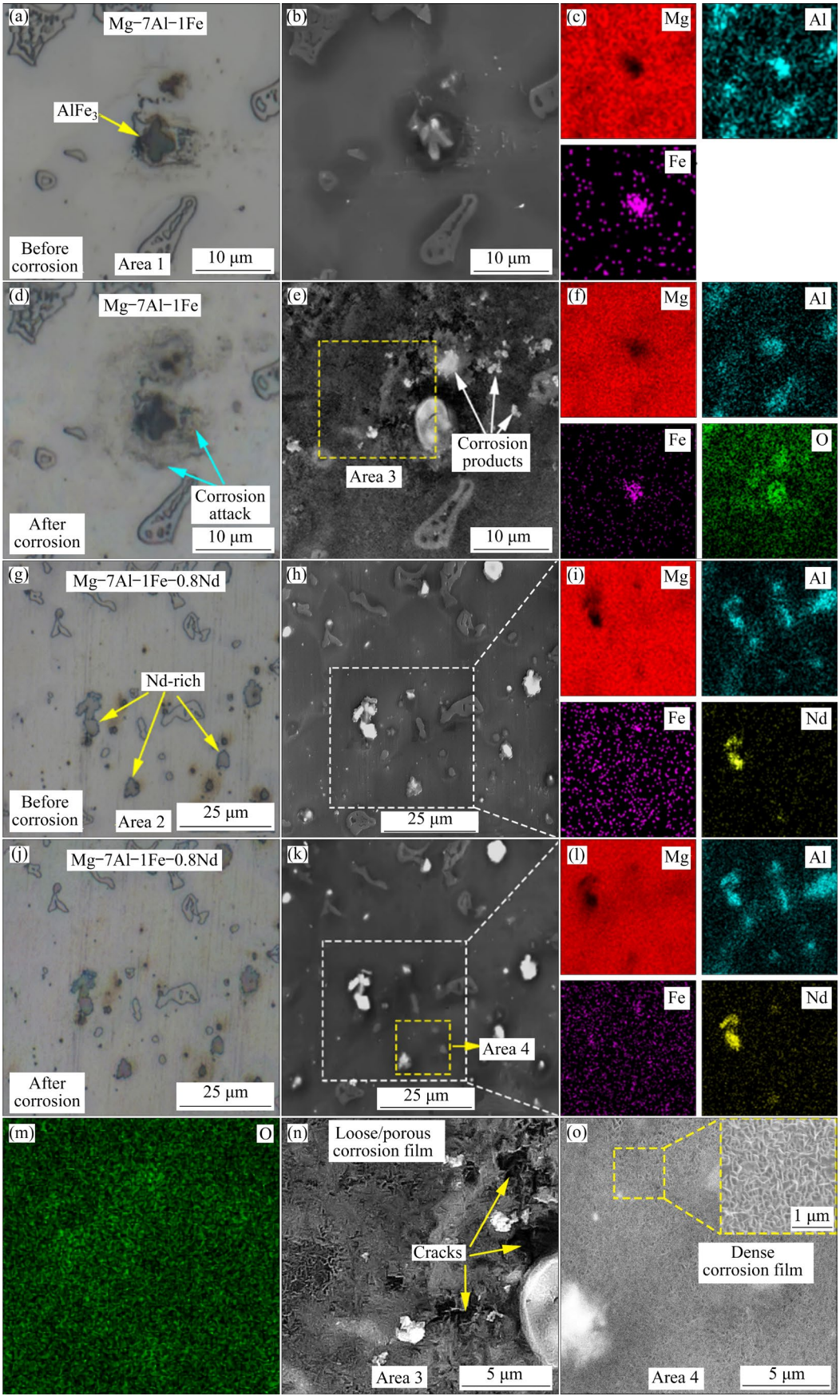

Fig. 10 OM (a, d, g, j), SEM (b, e, h, k, n, o) images and corresponding EDS maps (c, f, i, l, m) of Mg−7Al−1Fe−(0.8Nd) alloys before and after corrosion inside rectangle shown in Figs. 9(a, f, g, i): (a–f) Mg–7Al–1Fe alloy; (g–m) Mg–7Al–1Fe–0.8Nd alloy; (n, o) High-magnification images of (e) and (k), respectively

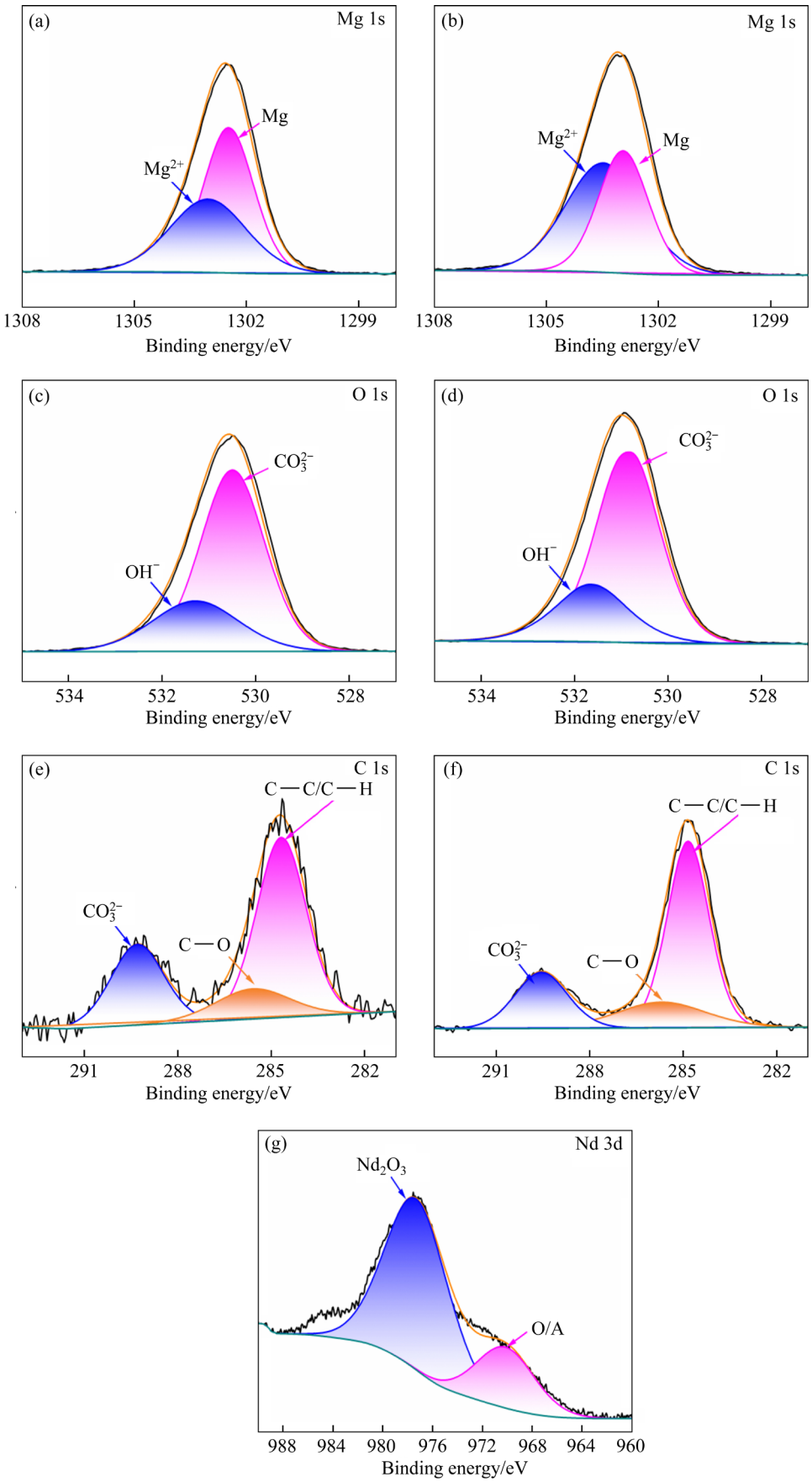

Fig. 11 XPS spectra of surface corrosive films after 24 h immersion in 0.6 mol/L NaCl solution; (a, c, e) Mg–7Al–1Fe alloy; (b, d, f, g) Mg–7Al–1Fe–0.8Nd alloy

the sample and electrolyte, which is believed to inhibit the erosion of harmful anions significantly.

3.3 Corrosion behaviour

Figure 12 shows the polarization curves of the tested alloys, and the electrochemical parameters derived by fitting the polarization curves are listed in Table 2. The corrosion potentials (φ_{corr}) of the Mg−7Al−1Fe, Mg−7Al−1Fe−0.4Nd, Mg−7Al−1Fe−0.8Nd, Mg−7Al−1Fe−1.2Nd, and Mg−9Al−1Fe−1Nd alloys were −1.49, −1.45, −1.40, −1.42 and −1.40 V (vs SCE), respectively. With an increase in Nd content, the φ_{corr} value of the alloys shifted positively. The most positive corrosion potential was obtained when the Nd content was 0.8, indicating that the Mg−7Al−1Fe−0.8Nd alloy exhibited the lowest corrosion driving force. The decreasing corrosion current density J_{corr} values of the alloys were arranged in the following order: Mg−7Al−1Fe > Mg−9Al−1Fe−1Nd > Mg−7Al−1Fe−0.4Nd > Mg−7Al−1Fe−1.2Nd > Mg−7Al−1Fe−0.8Nd. Notably, the Mg−7Al−1Fe−0.8Nd alloy exhibited the lowest current density and most positive corrosion potential.

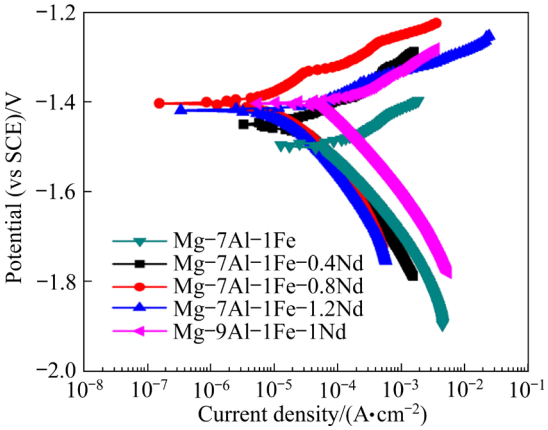

Fig. 12 Polarization curves of Mg−7Al−1Fe−xNd (x=0, 0.4, 0.8, and 1.2 wt.%) and Mg−9Al−1Fe−1Nd alloys in 0.6 mol/L NaCl solution

The EIS results of the tested alloys are shown in Fig. 13. The Nyquist plots (Fig. 13(a)) of all alloys consist of high-frequency capacitive, middle-frequency capacitive, and low-frequency inductive loops. The corresponding equivalent circuit and fitting data are shown in Fig. 13(a) and Table 3, respectively. In Table 3, R_s represents the solution

Table 2 Fitting parameters of Mg−7Al−1Fe−xNd (x=0, 0.4, 0.8, and 1.2 wt.%) and Mg−9Al−1Fe−1Nd alloys in potentiodynamic polarization curves

Specimen	φ_{corr}(vs SCE)/V	J_{corr}/(μA·cm^{-2})	β_a/(mV·dec^{-1})	β_c/(mV·dec^{-1})
Mg−7Al−1Fe	−1.49	112.2	83.3	−220.4
Mg−7Al−1Fe−0.4Nd	−1.45	41.6	102.5	−209.1
Mg−7Al−1Fe−0.8Nd	−1.40	9.2	82.1	−167.9
Mg−7Al−1Fe−1.2Nd	−1.42	18.0	51.5	−204.4
Mg−9Al−1Fe−1Nd	−1.40	91.8	85.0	−210.5

β_a and β_c represent anodic and cathodic Tafel slopes, respectively

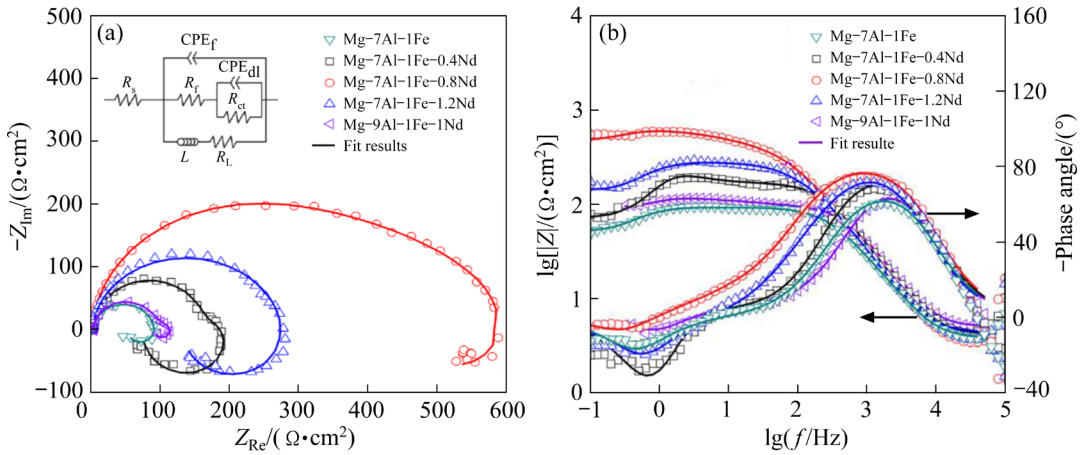

Fig. 13 EIS results of Mg−7Al−1Fe−xNd (x=0, 0.4, 0.8, and 1.2 wt.%) and Mg−9Al−1Fe−1Nd alloys in 0.6 mol/L NaCl solution: (a) Nyquist plots; (b) Bode plots

resistance. R_{ct} and CPE_{dl} indicate the charge transfer resistance and double-layer capacitance, respectively, used to reveal the high-frequency capacitive loop. R_f and CPE_f represent the surface film resistivity and capacitance, respectively, used to describe the middle-frequency capacitive loop. Because of the inhomogeneity of the tested alloy, ideal capacitors were replaced by constant-phase elements, which were defined by CPE and n. Furthermore, n is a discrete exponent, ranging from 0 to 1. For n=0, CPE is the ideal resistance and capacitance. The inductance resistance (R_L) and inductance (L) describe the inductive loop in the low-frequency range, which may be related to the desorption of corrosion products and the formation of pitting corrosion [40]. A corrosion-protective film that exhibits a high impedance modulus $|Z|$ at low frequencies is more effective, as shown in Fig. 13(b). The Mg−7Al−1Fe−0.8Nd alloy showed the largest R_{ct} value of 302.8 Ω·cm^2, indicating the optimum corrosion resistance. The Mg−7Al−1Fe−0.8Nd alloy displayed the largest R_f value of 351.1 Ω·cm^2, whereas the R_f value of the Mg–7Al–1Fe alloy was only 50.6 Ω·cm^2. In general, the higher the R_f value, the better the oxide film protection. Meanwhile, the Mg−7Al−1Fe−0.8Nd alloy exhibited the largest R_L of 1757.7 Ω·cm^2, implying the lowest tendency of pitting corrosion.

Figure 14(a) shows the hydrogen evolution and mass loss rates of the Mg−7Al−1Fe−xNd alloys over 10 and 24 h in a 0.6 mol/L NaCl solution, respectively. The corrosion rate calculated by hydrogen evolution and mass loss results are almost consistent, and the Mg−7Al−1Fe−0.8Nd alloy exhibits the lowest average corrosion rate (P_H=5.3 mm/a, P_W=5.8 mm/a). In addition, the Mg−7Al−1Fe alloy showed the highest hydrogen evolution rate, whereas the Mg−7Al−1Fe−0.8Nd alloy displayed the lowest hydrogen volume rate (Fig. 14(b)). The surface appearances of the tested alloys after immersion in 0.6 mol/L NaCl solution for 10 and 24 h are shown in Fig. 14(a). The appearance of the Mg−7Al−1Fe alloy was significantly attacked; however, slight corrosion occurred on the modified alloys. In addition, the Mg−7Al−1Fe−0.8Nd alloy exhibited the most

Table 3 Fitting parameters obtained from EIS data of Mg−7Al−1Fe−xNd (x=0, 0.4, 0.8, and 1.2 wt.%) and Mg−9Al−1Fe−1Nd alloys

Specimen	R_s/ (Ω·cm^2)	CPE_f/ (F·cm^{-2})	n for CPE_f	R_f/ (Ω·cm^2)	CPE_{dl}/ (F·cm^{-2})	N for CPE_{dl}	R_{ct}/ (Ω·cm^2)	L/ (H·cm^{-2})	R_L/ (Ω·cm^2)
Mg−7Al−1Fe	3.8	6.1×10^{-6}	0.98	50.6	2.1×10^{-5}	0.83	38.2	50.6	102.4
Mg−7Al−1Fe−0.4Nd	4.2	5.0×10^{-6}	0.98	161.5	1.6×10^{-3}	0.78	163.1	32.6	86.7
Mg−7Al−1Fe−0.8Nd	3.4	6.3×10^{-6}	0.97	351.1	2.7×10^{-4}	0.61	302.8	1077.1	1757.7
Mg−7Al−1Fe−1.2Nd	4.4	5.8×10^{-6}	0.98	195.0	8.4×10^{-5}	0.79	81.1	106.1	263.3
Mg−9Al−1Fe−1Nd	4.9	4.9×10^{-6}	0.97	942.0	2.9×10^{-4}	0.77	40.1	56.6	261.4

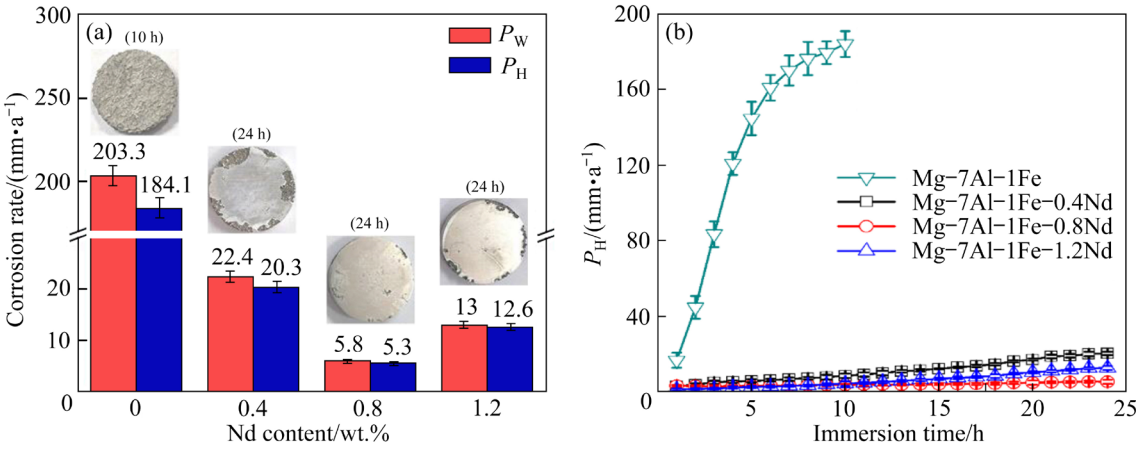

Fig. 14 Corrosion rates of tested alloys after immersion in 0.6 mol/L NaCl solution for 10 and 24 h, respectively (a), and hydrogen evolution rates of Mg−7Al−1Fe−xNd (x=0, 0.4, 0.8, and 1.2 wt.%) after immersion in 0.6 mol/L NaCl solution for different time (b)

complete surface, suggesting the optimum corrosion resistance. The addition of 0.4−0.8 wt.% Nd significantly reduced the corrosion attack, but a further increase in Nd content aggravated the corrosion slightly.

4 Discussion

In situ monitoring technology is vital for monitoring the micro-galvanic corrosion and electrochemical information of Mg alloys. Recently, TEM, SEM, SKPFM, and SVET techniques have been widely applied to investigating the corrosion mechanism of Mg alloys [17,20,28,29]. However, limited by the operating environment, these techniques cannot directly obtain the localized micro-galvanic corrosion process and the corresponding electrochemical kinetic information. Therefore, the localized micro-galvanic corrosion process and the corresponding electrochemical information were thoroughly investigated using in situ AFM, SKPFM combined with LSCM, and an electrochemical device integrated with OM in an actual electrolyte environment.

In this study, the $AlFe_3$ and Nd-rich phases enhanced and inhibited micro-galvanic corrosion in the Mg−(7,9)Al−1Fe−*x*Nd alloys, respectively, which was beneficial to characterizing the influence of the second phases during micro-galvanic corrosion by integrating a variety of in situ techniques. In situ AFM was used to monitor the corrosion morphology changes caused by localized micro-galvanic corrosion in the Mg−(7,9)Al−1Fe−*x*Nd alloys. Subsequently, SKPFM and LSCM were combined subtly, and bright white intermetallic particles were observed in both results. The results indicated that H_2 bubbles originated from the $AlFe_3$/*α*-Mg interface due to an intense galvanic couple formed between the $AlFe_3$ phase and the *α*-Mg matrix. In situ electrochemical OM successfully recorded the corrosion process and kinetic information of the Mg−7Al−1Fe−*x*Nd alloys in 0.6 mol/L NaCl solution. Subsequently, in situ OM combined with SEM was used to further investigate for localized micro-galvanic and corrosion products at the same position. Figure 15 shows the schematic diagrams of the corrosion mechanism of the tested alloys.

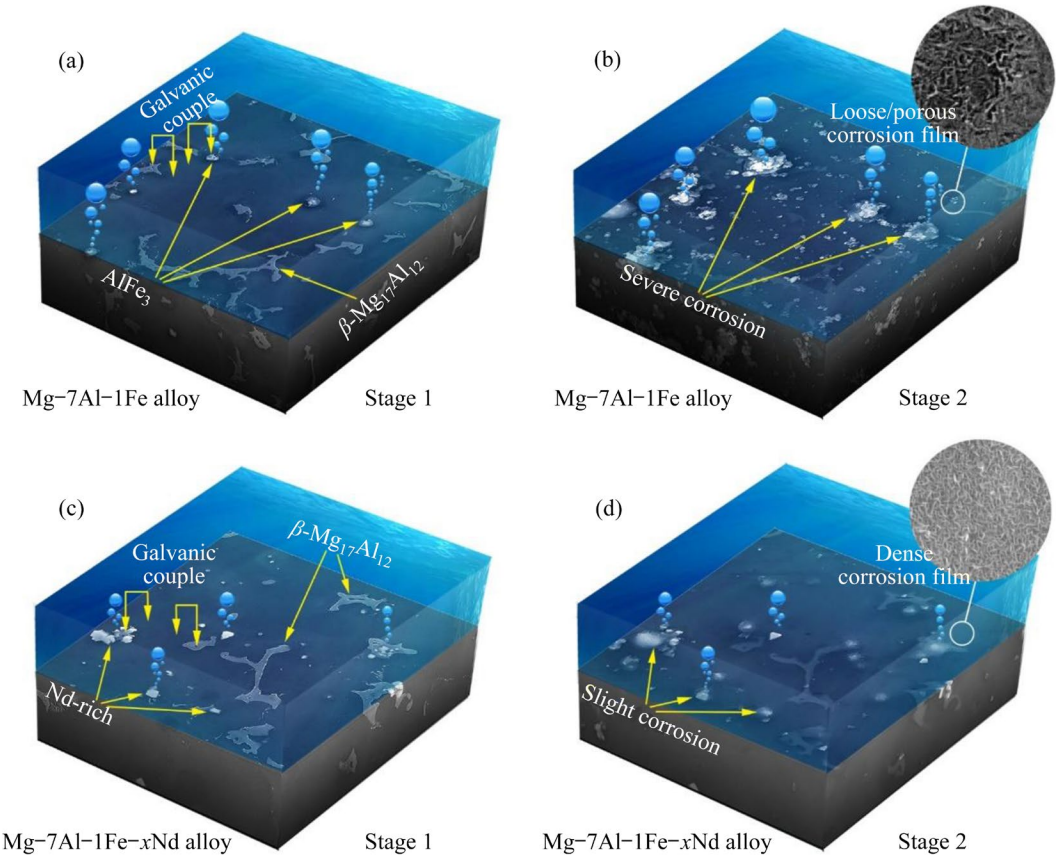

Fig. 15 Schematic diagrams of corrosion process in 0.6 mol/L NaCl solution: (a, b) Mg−7Al−1Fe alloy; (c, d) Mg−Al−1Fe−***x***Nd alloy

As shown in Fig. 15(a), there were two galvanic couples ($AlFe_3$/α-Mg and β-$Mg_{17}Al_{12}$/α-Mg) in Mg−7Al−1Fe alloy and the phase boundaries acted as the interface of the galvanic couples. When the alloy was immersed in NaCl electrolyte, Cl^- preferentially attacked the $AlFe_3$/α-Mg boundary owing to their large Volta potential difference (~400 mV). In situ LSCM results also indicated that localized corrosion initiated from α-Mg matrix contiguous to the $AlFe_3$ phase owing to a large Volta potential difference, accompanied by the generation of hydrogen bubbles, as shown in Fig. 4. The anode and cathode reactions involved the dissolution of magnesium ($Mg \rightarrow Mg^{2+}+2e$) and water reduction ($2H_2O+2e=H_2\uparrow+2OH^-$), respectively. Ultimately, $Mg(OH)_2$ was formed ($Mg^{2+}+2OH^-=Mg(OH)_2\downarrow$) near the cathode phase. Figure 15(b) shows Stage 2 of the corrosion process with increasing immersion time. Most corrosion products were observed near the $AlFe_3$ phase but less near the β-$Mg_{17}Al_{12}$ phase, in agreement with the corrosion behaviour of the $AlFe_3$ cathodic phase reported in the previous study [30]. The corrosion film of Mg−7Al−1Fe was loose and porous, which could not act as an effective protective film. Cl^- harms Mg alloys because it can easily pass through the $Mg(OH)_2$ film and reach the corrosion interface in solution. The porous corrosion film was ineffective in preventing Cl^- erosion, and the corrosion was further aggravated. Subsequently, the α-Mg matrix contiguous to the $AlFe_3$ phase was further corroded, and the corrosion gradually extended into the alloy. Some severe corrosion pits were ultimately formed near the $AlFe_3$ phase, accompanied by the aggregation of corrosion products and the formation of cracks, observed using SEM, as shown in Figs. 10(e) and (n). The matrix near the $AlFe_3$ phase was corroded preferentially, resulting in the loss of connection between the $AlFe_3$ phase and matrix, with a tendency for shedding. According to the in situ electrochemical OM results in Fig. 8(f), intense micro-galvanic corrosion may induce filiform corrosion with time, and then the filiform corrosion extends along the β-$Mg_{17}Al_{12}$ phase.

In the Mg−7Al−1Fe−***x***Nd alloy, less noble Nd-rich and β-$Mg_{17}Al_{12}$ phases acted as the cathodes of the micro-galvanic couples (Fig. 15(c)). It should be noted that slight corrosion occurred in the region adjacent to the Nd-rich phase, whereas no apparent corrosion attack was observed near the β-$Mg_{17}Al_{12}$ phase, as depicted in Stage 2 (Fig. 15(d)). The corrosion film of the modified alloy was complete and dense, which could effectively separate the metal matrix from corrosion solution and block the passage of Cl^-, as shown in Fig. 10(o). In situ AFM and in situ electrochemical OM observation results indicated that the morphology of the Nd-rich phase hardly changed with the immersion time, and only a tiny amount of corrosion products accumulated around the Nd-rich phase, as depicted in Figs. 6 and 9. Meanwhile, a passive region was found in the microscale potentiodynamic polarization curve in Fig. 7, which was attributed to the corrosion film containing Nd_2O_3. Additionally, according to the SKPFM results in Fig. 5, the potential difference of Nd-rich/α-Mg (~220 mV) was significantly lower than that of $AlFe_3$/α-Mg (~400 mV), but slightly higher than that of β-$Mg_{17}Al_{12}$/α-Mg (~150 mV). Consequently, the driving force of corrosion in the modified alloys was significantly reduced. The Mg−7Al−1Fe−0.8Nd alloy shows the optimum corrosion resistance, whereas Mg−7Al−1Fe−1.2Nd alloy presents a slightly worse corrosion resistance. Excessive Nd addition caused the formation of more Nd-rich phases in the Mg−7Al−1Fe−1.2Nd alloy, increasing corrosion sites. As the potential difference of Nd-rich/α-Mg (~220 mV) was higher than that of β-$Mg_{17}Al_{12}$/α-Mg (~150 mV), these excessive Nd-rich phases would slightly accelerate micro-galvanic corrosion [41,42].

5 Conclusions

(1) The Mg−7Al−1Fe alloy is composed of α-Mg matrix, β-$Mg_{17}Al_{12}$ and $AlFe_3$ phases. The addition of Nd to the Mg−7Al−1Fe alloy not only refines the β-$Mg_{17}Al_{12}$ phase, but also inhibits the cathode $AlFe_3$ phase.

(2) SKPFM results revealed that the potential difference of Nd-rich/α-Mg (~220 mV) was significantly lower than that of $AlFe_3$/α-Mg (~400 mV), but slightly higher than that of β-$Mg_{17}Al_{12}$/α-Mg (~150 mV). In situ LSCM results indicated that hydrogen bubbles originated from the matrix contiguous to the $AlFe_3$ phase. Combined with the SKPFM and LSCM results, micro-galvanic corrosion was preferentially initiated around the strong cathodic $AlFe_3$ phase.

(3) In situ AFM results indicated that the surface morphology of the Mg−9Al−1Fe−1Nd hardly changed during the immersion in NaCl solution, and only a few corrosion products were covered near the Nd-rich phase.

(4) The in situ electrochemical OM technique demonstrated that severe corrosion initiated at the $AlFe_3$/α-Mg boundary in Mg–7Al–1Fe alloy, which could induce filiform corrosion extending along the β-$Mg_{17}Al_{12}$ phase, but only slight corrosion occurred in Mg−7Al−1Fe−0.8Nd alloy. The current density of Mg−7Al−1Fe−0.8Nd was much smaller than that of Mg−7Al−1Fe alloy in the microscale potentiodynamic polarization tests.

(5) The Mg−7Al−1Fe−0.8Nd alloy presents the lowest current density (J_{corr}=9.2 μA/cm^2), the highest charge transfer resistance (R_{ct}= 302.8 Ω·cm^2) and the lowest average corrosion rate (P_H = 5.3 mm/a, P_W=5.8 mm/a).

CRediT authorship contribution statement

Kai-xuan FENG: Investigation, Methodology, Writing – Originial draft; **Tao LAI:** Methodology, Data curation; **Yang CHEN:** Data curation, Writing – Review & editing; **Zheng YIN:** Methodology, Data curation; **Zhi-qin WU:** Investigation, Data curation; **Hong YAN:** Conceptualization, Project administration, Writing – Review & editing; **Hong-gun SONG:** Resources, Writing – Review & editing; **Chao LUO:** Software, Resources, Writing – Review & editing; **Zhi HU:** Conceptualization, Methodology, Investigation, Validation, Data curation, Writing – Review & editing.

Declaration of competing interest

The authors declare that they have no known competing financial interests or personal relationships that could have appeared to influence the work reported in this paper.

Acknowledgments

The authors would like to acknowledge the financial support from the National Natural Science Foundation of China (No. 51961026).

References

[1] MORDIKE B L, EBERT T. Magnesium: Properties−applications−potential [J]. Materials Science and Engineering A, 2001, 302(1): 37−45.

[2] CZERWINSKI F. Controlling the ignition and flammability of magnesium for aerospace applications [J]. Corrosion Science, 2014, 86: 1−16.

[3] ZHANG Jing-huai, ZHANG Li, LENG Zhe, LIU Shu-juan, WU Rui-zhi, ZHANG Mi-lin. Experimental study on strengthening of Mg−Li alloy by introducing long-period stacking ordered structure [J]. Scripta Materialia, 2013, 68(9): 675−678.

[4] DU Jin-ying, WANG Guo-wei, SONG Dan, JIANG Jing-hua, JIANG Hong-bing, GAO Jun. In-vitro degradation behavior and biocompatibility of superhydrophilic hydroxyapatite coating on Mg−2Zn−Mn−Ca−Ce alloy [J]. Journal of Materials Research and Technology, 2022, 17: 2742−2754.

[5] KULEKCI M K. Magnesium and its alloys applications in automotive industry [J]. The International Journal of Advanced Manufacturing Technology, 2008, 39(9): 851−865.

[6] ZHANG Zhi, XIE Jin-shu, ZHANG Jing-huai, DONG Hao, LIU Shu-juan, ZHANG Xiao-bo, WANG Jun, WU Rui-zhi. Simultaneously improving mechanical and anti-corrosion properties of extruded Mg−Al dilute alloy via trace Er addition [J]. Journal of Materials Science & Technology, 2023, 150: 49−64.

[7] XU Shi-yuan, LIU Chu-ming, WAN Ying-chun, ZENG Guang, GAO Yong-hao, JIANG Shu-nong. Corrosion behaviour of Mg−Gd−Y−Zn−Ag alloy components with different sizes after cooling [J]. Transactions of Nonferrous Metals Society of China, 2021, 31(5): 1291−1302.

[8] XIE Jin-shu, WANG Le-le, ZHANG Jing-huai, LU Li-wei, ZHANG Zhi, HE Yu-ying, WU Rui-zhi. Developing new Mg alloy as potential bone repair material via constructing weak anode nano-lamellar structure [J]. Journal of Magnesium and Alloys, 2023, 11(1): 154−175.

[9] HE Shu-heng, WANG Ce, SUN Chao, ZHANG Yue, YAN Kai, JIANG Jing-hua, BAI Jing, XUE Feng, LIU Huan. Corrosion properties of ECAP-processed Mg−Al−Ca−Mn alloys with separate Al_2Ca and Mg_2Ca phases [J]. Transactions of Nonferrous Metals Society of China, 2022, 32(8): 2527−2540.

[10] NIE Yu-jin, DAI Jian-wei, LI Xuan, ZHANG Xiao-bo. Recent developments on corrosion behaviors of Mg alloys with stacking fault or long period stacking ordered structures [J]. Journal of Magnesium and Alloys, 2021, 9(4): 1123−1146.

[11] WANG Kai, LI Chen-pei, LI Yan-hui, LU Jin-ling, WANG Yue-she, LUO Xing-qi. Multi-physics analysis of the galvanic corrosion of Mg-steel couple under the influence of time-dependent anisotropic deposition film [J]. Journal of Magnesium and Alloys, 2021, 9(3): 866−882.

[12] KE LIU, LOU Feng, FU Jun-jian, YU Zi-jian, LI Shu-bo, WANG Zhao-hui, DU Xian, DU Wen-bo. Microstructure and corrosion behaviors of as-rolled Mg−Zn−Er alloy sheets [J]. Transactions of Nonferrous Metals Society of China, 2022, 32(6): 1881−1895.

[13] WANG Shuo, XU Dao-kui, WANG Dong-liang, ZHANG Zhi-qiang, WANG Bao-jie. Effect of icosahedral phase formation on the stress corrosion cracking (SCC) behaviors of the as-cast Mg−8%Li (in wt.%) based alloys [J]. Journal of Magnesium and Alloys, 2024, 12: 225−236.

[14] DONG Lin-jie, LIU Xi, LIANG Jie-xi, LI Chuan-qiang, DONG Yong, ZHANG Zheng-rong. Corrosion behavior of a

eutectic Mg−8Li alloy in NaCl solution [J]. Electrochemistry Communications, 2021, 129: 107087.

[15] XIE Jin-shu, ZHANG Jing-huai, ZHANG Zhi, YANG Qiang, GUAN Kai, HE Yu-ying, WANG Ru, ZHANG Hao, QIU Xin, WU Rui-zhi. New insights on the different corrosion mechanisms of Mg alloys with solute-enriched stacking faults or long period stacking ordered phase [J]. Corrosion Science, 2022, 198: 110163.

[16] XIE Jin-shu, ZHANG Jing-huai, ZHANG Zhi, YU Zi-jian, XU Zhi-hao, WANG Ru, FANG Da-qing, ZHANG Xiao-bo, ZHANG Xiao-ru, WU Rui-zhi. Corrosion mechanism of Mg alloys involving elongated long-period stacking ordered phase and intragranular lamellar structure [J]. Journal of Materials Science & Technology, 2023, 151: 190−203.

[17] HU Zhi, YIN Zheng, YIN Zhou, WANG Kun, LIU Qi-dong, SUN Peng-fei, YAN Hong, SONG Hong-gun, LUO Chao, GUAN Hong-yu. Corrosion behavior characterization of as extruded Mg−8Li−3Al alloy with minor alloying elements (Gd, Sn and Cu) by scanning Kelvin probe force microscopy [J]. Corrosion Science, 2020, 176: 108923.

[18] DOLEŽAL P, FOJT L, MINDA J. Methodology for in situ microstructural characterisation of AZ31 magnesium alloy corrosion degradation in Hanks' solution [J]. Materials Science Forum, 2017, 891: 298−302.

[19] CANO Z P, KISH J R, MCDERMID J R. On the evolution of cathodic activity during corrosion of magnesium alloy AZ31B in a dilute NaCl solution [J]. Journal of the Electrochemical Society, 2015, 163(3): 62−68.

[20] GNEDENKOV A S, SINEBRYUKHOV S L, MASHTALYAR D V, GNEDENKOV S V. Localized corrosion of the Mg alloys with inhibitor-containing coatings: SVET and SIET studies [J]. Corrosion Science, 2016, 102: 269−278.

[21] CHIBA A, MUTO I, SUGAWARA Y, HARA N. A micro-electrochemical system for in situ high-resolution optical microscopy: morphological characteristics of pitting at MnS inclusion in stainless steel [J]. Journal of the Electrochemical Society, 2012, 159(8): 341−350.

[22] ZHANG Li-na, JIA Rui-ling, LI Dan, ZHANG Wei, GUO Feng. Effect of intermetallic phases on corrosion initiation of AZ91 alloy with rare earth Y addition [J]. Journal of Materials Science & Technology, 2015, 31(5): 504−511.

[23] CUBIDES Y, KARAYAN A I, ZHAO D, NASH L, XIE K, CASTANEDA H. New insights on the corrosion mechanism of a peak-aged Mg−9Al−1Zn alloy in a chloride environment [J]. Journal of Alloys and Compounds, 2020, 840: 155786.

[24] LEIVA-GARCÍA R, GARCÍA-ANTÓN J, MUÑOZ-PORTERO M J. Contribution to the elucidation of corrosion initiation through confocal laser scanning microscopy (CLSM) [J]. Corrosion Science, 2010, 52(6): 2133−2142.

[25] SHI Yun-zhu, MO Jing-ke, ZHANG Feng-Yuan, YANG Bin, LIAW P K, ZHAO Ying. In-situ visualization of corrosion behavior of $Al_xCoCrFeNi$ high-entropy alloys during electrochemical polarization [J]. Journal of Alloys and Compounds, 2020, 844: 156014.

[26] HOMBORG A M, OLGIATI M, DENISSEN P J, GARCIA S J. An integral non-intrusive electrochemical and in-situ optical technique for the study of the effectiveness of corrosion inhibition [J]. Electrochimica Acta, 2022, 403: 139619.

[27] SHAO Zheng, NISHIMOTO M, MUTO I, SUGAWARA Y. Real-time in situ observation of the corrosion process of die-cast AZ91D magnesium alloy in NaCl solutions under galvanostatic polarization [J]. Corrosion Science, 2021, 192: 109834.

[28] XU Chen, WANG Jian-feng, CHEN Chen, WANG Chao, SUN Yu-feng, ZHU Shi-jie, GUAN Shao-kang. Initial micro-galvanic corrosion behavior between Mg_2Ca and α-Mg via quasi-in situ SEM approach and first-principles calculation [J]. Journal of Magnesium and Alloys, 2021, 9(3): 958−965.

[29] BAWANE K, LIU Xiao-yang, GAKHAR R, WOODS M, GE Ming-yuan, XIAO Xiang-hui, LEE W, HALSTENBERG P, DAI Sheng, MAHURIN S. Visualizing time-dependent microstructural and chemical evolution during molten salt corrosion of Ni−20Cr model alloy using correlative quasi in situ TEM and in situ synchrotron X-ray nano-tomography [J]. Corrosion Science, 2022, 195: 109962.

[30] SHEN Jun-ping, LAI Tao, YIN Zheng, CHEN Yang, WANG Kun, YAN Hong, SONG Hong-gun, LIU Rui-liang, LUO Chao, HU Zhi. In-situ AFM and quasi-in-situ studies for localized corrosion in Mg−9Al−1Fe−(Gd) alloys under 3.5 wt.% NaCl environment [J]. Journal of Magnesium and Alloys, 2022, 12: 1170−1185.

[31] YANG Lei, HE Shou-zhen, YANG Chao, ZHOU Xiao-rong, LU Xiao-peng, HUANG Yuan-ding, QIN Gao-wu, ZHANG E. Mechanism of Mn on inhibiting Fe-caused magnesium corrosion [J]. Journal of Magnesium and Alloys, 2021, 9(2): 676−685.

[32] YANG Lei, ZHOU Xiao-rong, LIANG Song-mao, SCHMID-FETZER R, FAN Zhong-yun, SCAMANS G, ROBSON J, THOMPSON G. Effect of traces of silicon on the formation of Fe-rich particles in pure magnesium and the corrosion susceptibility of magnesium [J]. Journal of Alloys and Compounds, 2015, 619: 396−400.

[33] YIN Zheng, CHEN Yang, YAN Hong, ZHOU Guo-hua, WU Xiao-quan, HU Zhi. Effects of the second phases on corrosion resistance of AZ91−xGd alloys treated with ultrasonic vibration [J]. Journal of Alloys and Compounds, 2019, 783: 877−885.

[34] ZOU Qi, LE Qi-chi, CHEN Xing-rui, JIA Yong-hui, BAN Chun-yan, WANG Tong, WANG He-nan, GUO Rui-zhen, REN Liang, ATRENS A. The influence of Ga alloying on Mg−Al−Zn alloys as anode material for Mg−air primary batteries [J]. Electrochimica Acta, 2022, 401: 139372.

[35] ARRABAL R, MATYKINA E, PARDO A, MERINO M C, PAUCAR K, MOHEDANO M, CASAJÚS P. Corrosion behaviour of AZ91D and AM50 magnesium alloys with Nd and Gd additions in humid environments [J]. Corrosion Science, 2012, 55: 351−362.

[36] JIANG Bin, XIANG Qing, ATRENS A, SONG Jiang-feng, PAN Fu-sheng. Influence of crystallographic texture and grain size on the corrosion behaviour of as-extruded Mg alloy AZ31 sheets [J]. Corrosion Science, 2017, 126: 374−380.

[37] GREEN B A, STEWARD R V, KIM I, CHOI C K, LIAW P K, KIHM K D, YOKOYAMA Y. In situ observation of pitting corrosion of the $Zr_{50}Cu_{40}Al_{10}$ bulk metallic glass [J].

Intermetallics, 2009, 17(7): 568−571.
[38] LI Xiao-jing, LIU Shu-hong, DU Yong. Investigation on the corrosion resistance of the Mg−10Al−*x*Mn alloys based on thermodynamic calculations [J]. Corrosion Science, 2021, 189: 109631.
[39] PEZZATO L, BABBOLIN R, CERCHIER P, MARIGO M, DOLCET P, DABALÀ M, BRUNELLI K. Sealing of PEO coated AZ91magnesium alloy using solutions containing neodymium [J]. Corrosion Science, 2020, 173: 108741.
[40] SUN Yue-hua, WANG Ri-chu, PENG Chao-qun, CAI Zhi-yong. Microstructure and corrosion behavior of as-extruded Mg−*x*Li−3Al−2Zn−0.2Zr alloys (*x*=5, 8, 11 wt.%) [J]. Corrosion Science, 2020, 167: 108487.
[41] ARRABAL R, PARDO A, MERINO M C, MOHEDANO M, CASAJÚS P, PAUCAR K, GARCÉS G. Effect of Nd on the corrosion behaviour of AM50 and AZ91D magnesium alloys in 3.5 wt.% NaCl solution [J]. Corrosion Science, 2012, 55: 301−312.
[42] YIN Zheng, HE Ren-hua, CHEN Yang, YIN Zhou, YAN Kun, WANG Kun, YAN Hong, SONG Hong-gun, YIN Cheng-xin, GUAN Hong-yu. Effects of surface micro-galvanic corrosion and corrosive film on the corrosion resistance of AZ91−*x*Nd alloys [J]. Applied Surface Science, 2021, 536: 147761.

Mg−(7,9)Al−1Fe−*x*Nd 合金的微电偶腐蚀行为

冯开轩[1]，赖 涛[1]，陈 扬[1]，殷 正[1]，吴志勤[1]，闫 洪[1]，宋红滚[1]，罗 超[1,2]，胡 志[1]

1. 南昌大学 先进制造学院，南昌 330031；
2. 南昌大学 高等研究院，南昌 330031

摘 要：采用电化学控制下的原位观察和原位原子力显微镜研究 Mg−(7,9)Al−1Fe−*x*Nd 合金在电解液环境下的局部微电偶腐蚀过程及动力学信息。结果表明：合金中富 Nd 相的形成导致电位差从~400 mV ($AlFe_3$/*α*-Mg) 降低到~220 mV (富 Nd 相/*α*-Mg)，使阴极相周围腐蚀产物减少、微尺度区域腐蚀电流密度降低。添加 Nd 显著提高了材料的耐蚀性能，主要归因于第二相与基体之间微电偶腐蚀的抑制。最后，根据原位观察和电化学结果讨论了 Mg−(7,9)Al−1Fe−*x*Nd 合金的腐蚀机理。

关键词：镁合金；扫描开尔文探针显微镜；微电偶腐蚀；原位观察；原子力显微镜

(Edited by Wei-ping CHEN)